TIME-DEPENDENT ACCRETION ONTO MAGNETIZED WHITE DWARFS

STEVEN H. LANGER
Joint Institute for Laboratory Astrophysics, University of Colorado and National Bureau of Standards

G. CHANMUGAM
Department of Physics and Astronomy, Louisiana State University

AND

G. SHAVIV
Faculty of Physics, Israel Institute of Technology

ABSTRACT

We consider time-dependent accretion onto magnetized white dwarfs. A detailed description of a numerical method of solution to the hydrodynamical equations is given. The postshock flow is cooled by optically thin bremsstrahlung and is thermally unstable. As a result the shock height undergoes periodic oscillations. We consider the properties of this oscillation as a function of the accretion rate and of the mass and radius of the white dwarf. The structure of the accretion flow depends on a single scaling parameter. Below a critical accretion rate, which depends on the particular white dwarf, the nature of the accretion flow changes and the shock propagates up the accretion column indefinitely.

Subject headings: hydrodynamics — stars: accretion — stars: magnetic — stars: white dwarfs — X-rays: binaries

I. INTRODUCTION

The pulsating binary X-ray sources have been the object of intense observational and theoretical study since their discovery more than a decade ago (Giacconi *et al.* 1971). The generally accepted model of the binary X-ray sources consists of a compact object (white dwarf, neutron star, or black hole) accreting matter from a companion star that is on or near the main sequence (see, e.g., Lamb, Pethick, and Pines 1973). The X-rays are emitted when the kinetic energy of the infalling matter is thermalized in a shock, or in some other fashion, near the surface of the accreting object. If the compact object is a neutron star or white dwarf with a strong magnetic field, the accretion flow is channeled onto the polar caps where it produces small, bright patches as the accretion energy is released. As the star rotates, these spots pass in and out of the line of sight and produce X-ray pulsations.

The first of the pulsating X-ray sources to be discovered were the X-ray pulsars (Giacconi *et al.* 1971). These systems contain a rotating, magnetized neutron star which emits most of the accretion luminosity in the form of hard (1–20 keV) X-rays. X-ray binary systems containing white dwarfs were not discovered until somewhat later (Rappaport *et al.* 1974; Hearn and Richardson 1977), for two reasons. First, they have a gravitational potential 10^3 times less than a neutron star and thus are much less luminous for a given accretion rate. Second, most of their luminosity is emitted in the extreme-ultraviolet and soft X-ray bands (Tuohy *et al.* 1978; Raymond *et al.* 1979), where it is quite difficult to observe. Nevertheless, several of these systems have now been discovered and may be classified into three distinct groups. One group is comprised of the AM Herculis variables which contain a white dwarf with a magnetic field $B \sim 10^7$ gauss (Visvanathan and Wickramasinghe 1979; Schmidt, Stockman, and Margon 1981) and emit strongly polarized optical radiation by the cyclotron emission process. The strong magnetic field prevents the formation of an accretion disk and forces the white dwarf to rotate synchronously (see Chiappetti, Tanzi, and Treves 1980, and references therein). A second group contains systems such as H2252 (Patterson and Price 1981) and AE Aquarii (Patterson *et al.* 1980) that probably contain a white dwarf which is rotating much faster than synchronously. These systems exhibit hard X-ray pulsations and optical pulsations due to reprocessing of X-rays in the atmosphere of the companion star. Finally, the third group contains systems such as SS Cyg and U Gem that show clear optical evidence of an accretion disk (Kiplinger 1979; Fabbiano *et al.* 1981). In these systems the magnetic field of the white dwarf is quite weak, and the accretion disk may extend all the way down to the surface of the white dwarf (Ricketts, King, and Raine 1979; cf. Pringle and Savonije 1979). These three types of systems are all classified as cataclysmic variables and have unusual optical spectra which contain considerable information about the accretion disk, when one exists. In this paper we are interested in the energy released at the surface of the white dwarf, which comes out primarily in the form of extreme-ultraviolet, soft X-rays and hard X-rays.

Theoretical models of these systems must address the question of how the kinetic energy of the infalling material is thermalized, determine the velocity, density, and temperature in the flow, calculate the emitted radiation at all frequencies, and consider the effects of radiative transfer. In general these effects are coupled together, making a full solution difficult. As a result, theoretical calculations of the spectra from nonmagnetic white dwarfs (e.g., Cameron and Mock 1967; Hōshi 1973; Aizu 1973; Katz 1977) and magnetic white dwarfs (Fabian, Pringle, and Rees 1976; King and Lasota 1979; Lamb and Masters 1979; Chanmugam and Wagner 1979) have not included full solutions to the hydrodynamics or the radiative transfer. Numerical solutions of the hydrodynamical equations have been presented for spherical accretion (Kylafis and Lamb 1979) and for steady state flow onto magnetic white dwarfs (Wada et al. 1980).

In an earlier paper (Langer, Chanmugam, and Shaviv 1981, hereafter Paper I), we presented the first time-dependent numerical solutions to the hydrodynamical equations for accretion onto a white dwarf. We demonstrated that the shock height underwent a periodic limit cycle due to a thermal instability in the bremsstrahlung-dominated cooling. In this paper we describe in detail our method of solution and consider a wide range of accretion rates and white dwarf masses and radii. Our results demonstrate the dependence of the maximum shock height and the period of the limit cycle on the system parameters. We present a scaling law which shows that the structure of the accretion flow depends, for the cases we consider, on a single parameter which contains the properties of the white dwarf and the accretion rate. We also find that there is a critical accretion rate (for a magnetized white dwarf), below which any shock that forms moves up the accretion column indefinitely (see Langer and Rappaport 1982 for a discussion of a similar phenomenon).

This paper is organized as follows. In § II we discuss the importance of various physical processes in the accretion flow and justify several simplifying assumptions made in the calculation. In § III and the Appendices we present the numerical method used to solve the hydrodynamic equations. In § IV we present flow solutions for several different sets of system parameters. Section V contains a discussion of the results and derives several important properties of the flow solutions. Finally, we summarize our principal results in § VI.

II. PHYSICAL SCALES

In this section we first estimate some of the physical quantities characterizing the accretion column of the white dwarf. We then use these to discuss the characteristic relaxation and cooling time scales in the current problem and the relative importance of various radiative and dissipative processes. These estimates demonstrate that we can make several simplifying approximations to the physical processes occurring in the accretion flow.

The free-fall velocity of the accreting material, as a function of the distance r from the center of the white dwarf of mass M and radius R, is given by

$$V_{\rm ff}(r) = 5.2 \times 10^8 \left(\phi \frac{R}{r} \right)^{1/2} \ {\rm cm\ s^{-1}} , \qquad (1)$$

where $\phi \equiv (M/M_\odot)(R/10^9 \ {\rm cm})^{-1}$. A characteristic free-fall time is given by

$$t_{\rm ff}(r) = r/V_{\rm ff}(r) = 1.9 \left(\frac{r}{R} \right)^{3/2} \phi^{-1/2} R_9 \ {\rm s} . \qquad (2)$$

where $R_9 \equiv R/10^9$ cm.

The accretion luminosity is $L = GM\dot{M}/R$, where $\dot{M}$ is the mass accretion rate, so that

$$\dot{M} = 7.5 \times 10^{16} \phi^{-1} L_{34} \ {\rm g\ s^{-1}} , \qquad (3)$$

where $L_{34} = L/10^{34}$ ergs s^{-1}. The typical luminosities observed in the AM Her binaries are of order 10^{32}–10^{34} ergs s^{-1} and depend on the particular system and its state (e.g., "high" or "low") (Chiappetti, Tanzi, and Treves 1980). For a spherically symmetric star and an opacity dominated by Thomson scattering, the downward force of gravity and the upward radiation force are equal when L is equal to the Eddington luminosity ($1.25 \times 10^{38} M/M_\odot$ ergs s^{-1} for a hydrogen plasma). Because of magnetic confinement, accretion occurs over only about 0.001 of the surface, so that the amount of luminosity needed to reach the Eddington flux (given above for the case where the flux flows out over 4π steradians) is reduced by a factor of 1000. In spite of this extra factor, radiation pressure is still unimportant for the problem under consideration (cf. Davidson 1973).

We shall assume that the cross-sectional area of the accretion column, A, and the physical properties of the gas are a function only of r and that near the star

$$A = A_{\rm cap}(r/R)^s \qquad (4)$$

where the constant $s = 3$ for a dipolar magnetic field, and $s = 2$ for spherically symmetric accretion in the absence of a magnetic field. The area of the polar cap is roughly 0.001–0.01 of the stellar surface for the AM Her systems and might reach 0.1 for systems with weaker magnetic fields (Fabbiano et al. 1981).

If the free-falling gas consists of ionized hydrogen, the electron number density in the region above the shock is given by

$$n_{\rm ff} = \dot{M}/(m_p A V_{\rm ff})$$
$$= 1.2 \times 10^{15} \phi^{-1/2} \Psi \left(\frac{r}{R} \right)^{-s+1/2} \ {\rm cm^{-3}} , \qquad (5)$$

where $\Psi \equiv (\dot{M}/10^{16} \ {\rm g\ s^{-1}})(10^{16} \ {\rm cm^{12}}/A_{\rm cap})$. The accreting gas passes through a strong shock near the surface of the white dwarf. If we consider a stationary shock, the postshock gas attains a temperature $T_{\rm sh}$ given by (see, e.g., Hōshi 1973)

$$k_{\rm B} T_{\rm sh} = 3GM\mu/(8R) = 26.1\phi \ {\rm keV} = 3 \times 10^8 \phi k_{\rm B} \ {\rm K} , \qquad (6)$$

where $\mu = m_p/2$ is the mass per particle, for ionized

hydrogen. For a strong stationary shock, the postshock speed of the accreting material is $V_{ff}/4$, and the electron number density is 4 times the value given in equation (5).

In our calculations we assume that the electrons and protons have Maxwellian distributions characterized by the same temperature. In order to determine whether this is justified, we estimate the time for a proton of thermal velocity $V = (3k_B T/m_p)^{1/2}$ to be deflected by 90° through Coulomb scattering in a hydrogen plasma (see, e.g., Spitzer 1956),

$$t_D = 6.1 \times 10^{-5} T_8^{3/2} n_{16}^{-1} (20/\ln \Lambda_c) \text{ s} , \quad (7)$$

where $T_8 = T/10^8$ K, $n_{16} = n_e/10^{16}$ cm^{-3}, and the Coulomb logarithm is

$$\ln \Lambda_c = 18.6 + \ln (T_8^{3/2} n_{16}^{-1/2}) . \quad (8)$$

The mean free path of a proton is thus $\sim 10^4$ cm, which is much less than the height h of the shock front above the surface of the white dwarf (see below), and the protons may be assumed to have a Maxwellian velocity distribution.

If the electrons and protons have Maxwellian velocity distributions, with temperatures T_e and T_p respectively, the time required to establish equilibrium between them is (Spitzer 1956)

$$t_{eq} = 3/8(2\pi)^{-1/2} m_e m_p k_B^{3/2}$$
$$\times (T_e/m_e + T_p/m_p)^{3/2}/(n_e e^4 \ln \Lambda_c) . \quad (9)$$

If $T_e/m_e \gg T_p/m_p$,

$$t_{eq} = 1.3 \times 10^{-3} \left(\frac{T_e}{10^8 \text{ K}}\right)^{3/2} n_{16}^{-1} \left(\frac{20}{\ln \Lambda_c}\right) \text{ s} . \quad (10)$$

In evaluating t_{eq} we have neglected the effects of the magnetic field. For fields $B \sim 10^8$ gauss, the corrections to the Coulomb logarithm are of the order of unity and hence do not change the above rough estimate significantly (see, e.g., Masters 1978).

In our model we assume that the dominant cooling mechanism is optically thin bremsstrahlung radiation. We, therefore, compare the strength of bremsstrahlung and cyclotron emission to see when this assumption is valid. Most of the bremsstrahlung radiation from the shock-heated region is in the form of X-rays, which are not absorbed in the accretion column (see below). Thus, we use the optically thin approximation in deriving the bremsstrahlung cooling time:

$$t_{br} = \tfrac{3}{2}(n_e + n_p)k_B T/(C_{br} n_e n_p T^{1/2}) = 0.3 T_8^{1/2}/n_{16} \text{ s} , \quad (11)$$

where $C_{br} = 1.4 \times 10^{-27}$, in cgs units, for a hydrogen plasma (Allen 1973). This shows that $t_{br} \gg t_{eq}, t_D$, and the plasma equilibrates before it cools.

The ratio of the bremsstrahlung cooling time to the free-fall time *above the shock* is given, using equations (2), (5), and (11), by

$$\frac{t_{br}}{t_{ff}} = 1.3 \left(\frac{r}{R}\right)^{s-2} T_8^{1/2} \phi R_9^{-1} \Psi^{-1} . \quad (12)$$

Hence bremsstrahlung cooling is strong enough to ensure that the preshock flow is cooled, so that no adiabatic heating takes place. The low preshock temperature has no effect on the postshock conditions and ensures hypersonic flow that approaches free-fall above the shock.

Due to the strong magnetic field of the white dwarf, the emission of cyclotron radiation can be an important cooling mechanism. An optically thin plasma emits very strongly at the fundamental harmonic of the cyclotron line and would have a cooling time much shorter than any other cooling or flow time in the problem. However, the cyclotron radiation is strongly self-absorbed for frequencies up to $\omega^* \sim 10\omega_c$, where ω_c is the cyclotron frequency (Chanmugam and Wagner 1979; Lamb and Masters 1979). If we assume that the flux follows a Rayleigh-Jeans curve up to ω^* and is negligible for higher frequencies, the cyclotron luminosity from a plasma slab of thickness x, surface area A, and uniform temperature T is

$$L_{cyc} = \frac{A k_B T}{12\pi^2 c^2} [\omega^*(x)]^3 ,$$

where the angle-averaged cyclotron opacity has been used. Thus, provided that the flux out the sides of the column can be ignored, this equation shows how the luminosity increases as the plasma layer is made thicker. The cyclotron cooling of each layer of the column is the difference between a Rayleigh-Jeans flux extending to $\omega^*(x)$ and $\omega^*(x + dx)$, where x is now the distance from the shock. Thus,

$$\frac{dL_{cyc}}{dx} = \frac{A k_B T}{4\pi^2 c^2} \omega^{*2} \frac{d\omega^*}{dx} . \quad (13)$$

Wada *et al.* (1980) have provided a simple fit to $m^* \equiv \omega^*/\omega_c$ based on the results of Chanmugam and Wagner (1979):

$$m^* = 9.87 \Lambda_7^{0.05} T_8^{1/2} , \quad (14)$$

where the dimensionless parameter $\Lambda = 4\pi e n_e x/B$ and $\Lambda_7 = \Lambda/10^7$. This agrees to within $\sim 15\%$ with the fit given by Masters (1978), in the range considered. From equations (13) and (14) it follows that

$$\frac{dL_{cyc}}{dx} = \frac{A k_B T \omega^{*3}}{80\pi^2 c^2 x} . \quad (15)$$

The ratio of bremsstrahlung to cyclotron cooling rates can be calculated using equations (11), (14), and (15). For a plasma with $k_B T = 20$ keV, we find

$$\frac{t_{cyc}}{t_{br}} = \frac{3}{2} \frac{A(n_e + n_p)k_B T}{t_{br}} \left(\frac{dL_{cyc}}{dx}\right)^{-1}$$
$$= 1.1 \times 10^2 n_{16}^{1.85} x_7^{0.85} B_7^{-2.85} T_8^{-2} , \quad (16)$$

where $x_7 = x/10^7$ cm, and $B_7 = B/10^7$ gauss. Thus, cyclotron cooling is important for large magnetic fields and close to the shock (where x is small). We consider systems where B is not particularly large and are willing

to accept errors in the cooling close to the shock. Thus, in this paper, we ignore cyclotron emission.

We have assumed that all radiation emitted in the accretion column escapes freely. To determine the validity of this approximation we consider the three major sources of opacity: cyclotron absorption, free-free absorption, and Thomson scattering. We find that all three can be important at different places in the flow and for different frequencies. The electron-scattering optical depth across the column is

$$\tau_{es} = (A/\pi)^{1/2} n_e(r) \sigma_T , \qquad (17)$$

where σ_T is the Thomson scattering cross section. For a density equal to the postshock density, the optical depth is

$$\tau_{es} = 0.18 \phi^{-1/2} \Psi \left(\frac{A_{cap}}{10^{16} \text{ cm}^2} \right)^{1/2} (R/r)^{(s-1)/2} , \quad (18)$$

so that the column may be thick to electron scattering.

The free-free absorption coefficient is given by

$$a_{ff}(v) = 3.7 \times 10^8 v^{-3}$$
$$\times [1 - \exp(-hv/k_B T)] T^{-1/2} n_e^2 \text{ cm}^{-1} , \quad (19)$$

where v is the frequency of the radiation and the Gaunt factor has been chosen as equal to 1 (Allen 1973). For $T \sim 10^6$ K, optical radiation would be absorbed if the path length were greater than 10^7 cm (this is relevant to the region above the shock). However, if the temperature were higher, e.g., $k_B T \sim 10$ keV, it would require path lengths greater than 10^{10} cm to produce free-free absorption of optical radiation. For densities less than $\sim 10^{19}$ cm^{-3}, 1 keV X-rays are not absorbed unless the path length exceeds 10^9 cm. We can thus ignore absorption of hard X-rays everywhere except in the white dwarf atmosphere.

The height of the shock-heated region, h, is roughly 10^6–10^8 cm (Lamb and Masters 1979, also see below), while the diameter of the accretion column near the surface of the white dwarf is probably $\sim 10^8$ cm (Fabbiano et al. 1981). Thus, there is no free-free absorption of X-radiation in the accretion column, confirming the use of optically thin bremsstrahlung for the cooling. Optical radiation may undergo cyclotron absorption below the shock and free-free absorption above the shock. For the models considered in this paper the optical luminosity is negligible, so we ignore optical radiation and absorption.

We next consider the effects of heat conduction and viscosity. The energy transported out of the shock-heated region by heat conduction is

$$L_{heat} \sim A K_{cond} \frac{dT}{dr} , \qquad (20)$$

where the thermal conductivity is

$$K_{cond} = 10^{-6} T^{2.5} \text{ ergs cm}^{-1} \text{ s}^{-1} \text{ K}^{-1} \qquad (21)$$

(Allen 1973). The crude approximation $dT/dr \sim T/h$

permits a comparison of L_{heat} and the bremsstrahlung losses L_{br}:

$$L_{heat}/L_{br} = 7.1 \times 10^{-2} T_8^3 / (h_7^2 n_{16}^2) , \qquad (22)$$

showing that $L_{heat} < L_{br}$ if $h \gtrsim 3 \times 10^6$ cm (for $T_8 = n_{16} = 1$). Heat conduction is important only for accretion rates which produce a shock that is close enough to the surface that the conductive heat flux is a significant fraction of the accretion luminosity.

The viscous heating per unit volume is roughly

$$\mu_{vis} v^2 / h^2 , \qquad (23)$$

where the viscosity

$$\mu_{vis} = 2.2 \times 10^{-15} T^{2.5} / \ln \Lambda_c \text{ g cm}^{-1} \text{ s}^{-1} . \quad (24)$$

The total viscous heating in the shock-heated region is $\sim 10^{30}$ ergs s^{-1}, which is negligible.

III. THE MODEL

If the electron and ion temperatures remain the same throughout the flow (see eqs. [7] and [10]), the hydrodynamic equations are (see Rotty 1962; we have included the gravitational field, radiative losses, viscosity, and heat conduction)

$$\frac{\partial m}{\partial t} = -\frac{\partial k}{\partial r} ,$$

$$\frac{\partial k}{\partial t} = -\frac{\partial}{\partial r} \frac{k^2}{m} - A \frac{\partial}{\partial r} (p - \sigma) - \frac{GM}{r^2} m ,$$

$$\frac{\partial E}{\partial t} = -\frac{\partial}{\partial r} \left[\frac{k}{m} (E + pA - \sigma A) + JA \right] - \frac{m^2}{4\mu^2 A} \epsilon_{rad} . \quad (25)$$

In these equations,

$$m \equiv \rho A , \quad k \equiv \rho v A ,$$

$$E \equiv \frac{1}{2} \frac{k^2}{m} - \frac{GM}{r} m + \frac{3}{2} \frac{m}{\mu} k_B T , \qquad (26)$$

where ρ is the mass density, v is the flow velocity (positive outward), T is the temperature, μ is the mass per particle (half the proton mass for a hydrogen plasma), p is the gas pressure, k_B is Boltzmann's constant, J is the energy flux transferred by heat conduction, and σ is the viscous stress. The forms of the dissipative terms J and σ are discussed in Appendix A. The final term in the energy equation represents the radiative losses.

For optically thin thermal bremsstrahlung, ϵ_{rad} is given by $\epsilon_{br} = C_{br} T^{1/2}$ ergs cm^3 s^{-1} for a hydrogen plasma, with T measured in Kelvins (see eq. [11]). The value of ϵ_{rad} for cyclotron emission, including the effects of optical thickness, is discussed in § II.

We solve the flow equations numerically by evaluating the solution at a grid of points and approximating the derivatives by finite differences. We impose boundary conditions of zero mass flux through the lower boundary and require that the accreting gas be in free-fall with a large Mach number (>10) and a density corresponding to $\dot{M}$ at the upper boundary. To prevent numerical

instabilities we include artificial viscosity and heat conduction and apply a filter to the solution. These terms act to remove fluctuations on the scale of 1 or 2 mesh points, which are in principle too fine for the numerical solution to determine.

The details of the finite difference method and the filter are presented in the Appendices. However, we summarize several key points here. There are many ways to write finite difference representations of a set of differential equations which are accurate to a given order. We have taken advantage of this freedom to impose several constraints on the difference equations. The first establishes mass conservation to within the precision of the computer. Energy is not conserved to the same accuracy because of the form of the filter (see Appendices). We have also chosen forms of the equations which have analytic solutions for free-fall and a hydrostatic, isothermal atmosphere. The advantage of this is that we may choose an initial solution which does not need to relax before the interesting portions of the flow can be studied.

We also employ an implicit form of the difference equations. This means that the terms on the right of equations (25) are evaluated in terms of the flow variables at the end of the current time step. This is a standard technique for improving the numerical stability of the equations and therefore permitting the use of larger time steps. In spite of the many orders of magnitude by which the temperature, density, and velocity change across the model, we have found that approximately 100 mesh points provide adequate coverage of the solution if their locations are properly chosen.

The combination of the Shuman filter (see Appendix B) and artificial dissipation prevents the growth of numerical instabilities in the solution. We have reduced the strength of the artificial dissipation to the minimum value necessary to prevent the formation of instabilities and have chosen functional forms such that the dissipation acts only over small portions of the flow. The solutions are insensitive to moderate increases in the strength of the dissipation above the chosen values, thus indicating that these dissipative terms have a negligible effect on the solution.

We may recast the hydrodynamic equations (25) in dimensionless form by defining $\tilde{r} \equiv r/R$, $\tilde{t} \equiv tv_*/R$, $\tilde{m} \equiv mv_*/\dot{M}$, $\tilde{k} \equiv k/\dot{M}$, $\tilde{E} \equiv E/(\dot{M}v_*)$, $\tilde{p} \equiv pA_{\rm cap}/(\dot{M}v_*)$, $\tilde{J} \equiv JA_{\rm cap}/(\dot{M}v_*^2)$, and $\tilde{\sigma} \equiv A_{\rm cap}/(\dot{M}v_*)$, where $v_* \equiv (2GM/R)^{1/2}$. The resulting equations are

$$\frac{\partial \tilde{m}}{\partial \tilde{t}} = -\frac{\partial \tilde{k}}{\partial \tilde{r}},$$

$$\frac{\partial \tilde{k}}{\partial \tilde{t}} = -\frac{\partial}{\partial \tilde{r}}\frac{\tilde{k}^2}{\tilde{m}} - \tilde{r}^s\frac{\partial}{\partial \tilde{r}}(\tilde{p} - \tilde{\sigma}) - \frac{\tilde{m}}{2\tilde{r}^2},$$

$$\frac{\partial \tilde{E}}{\partial \tilde{t}} = -\frac{\partial}{\partial \tilde{r}}\left\{\frac{\tilde{k}}{\tilde{m}}[\tilde{E} + \tilde{r}^s(\tilde{p} - \tilde{\sigma})] + \tilde{r}^s\tilde{J}\right\} - \frac{\dot{M}R\tilde{m}^2}{4\mu^2 Av_*^4}\epsilon_{\rm rad}.$$

$$(27)$$

An important special case occurs when both heat con-

duction and viscosity are unimportant. Then the system parameters are contained solely in the term containing $\epsilon_{\rm rad}$ in equation (27). If we further assume that bremsstrahlung radiation dominates the cooling, this term becomes $C_1\tilde{m}^2\tilde{T}^{1/2}/\tilde{r}^s$, where $\tilde{T} \equiv T/T_*$, $T_* \equiv GMm_p/(Rk_{\rm B})$, and

$$C_1 = 0.29\Psi R_9\phi^{-3/2}\left(\frac{m_p}{2\mu}\right)^2. \qquad (28)$$

The differential equation has a one-parameter (C_1) set of solutions, if the boundary conditions (in dimensionless form) do not depend on the system parameters. The upper boundary condition of cold gas in free fall does not contain the system parameters. The lower boundary condition serves primarily to determine the point where the cooling gas comes to a halt and thus, in some sense, simply determines R_9. The equations indicate, and the models show, that the dimensionless solutions depend only on C_1. By adding the proper dimensions, solutions obtained for one choice of ϕ can be used to determine the solutions for another ϕ.

IV. RESULTS

We have studied the behavior of the accretion flow for several different accretion rates and white dwarf parameters. In all cases we choose an initial model where the gas is in free fall well above the surface of the white dwarf and then smoothly joins onto a hydrostatic white dwarf atmosphere. The results should not depend on the initial conditions, so we are free to use this convenient starting point.

We have used a polar cap area $A_{\rm cap} = 10^{16}$ cm^2 in all of our models. It is shown in § III that the solutions depend only on the combination $\dot{M}/A_{\rm cap}$, for a particular white dwarf, so this assumption does not restrict the validity of our results. We have considered several models with $R \sim 10^9$ cm, $M \sim M_\odot$. Figure 1 shows the velocity, density, pressure, temperature, and radiative losses as a function of radius at a time when the shock height was $\sim 20\%$ of the white dwarf radius. In this model $R = 10^9$ cm, $M = 0.5\ M_\odot$, and $\dot{M} = 2.5 \times 10^{15}$ g s^{-1}. The density jumps by a factor of 4 across the shock, while the velocity drops by a factor of 10, and the temperature jumps to 2×10^8 K. This is a strong shock, but the velocity does not drop by a factor of 4 as in the usual Rankine-Hugoniot relation. This is because the shock is moving upward (with a speed $\sim V_{\rm ff}/5$), and the jump conditions apply in the frame where the shock is stationary.

Behind the shock there is a fairly thick region of material at the postshock temperature which is falling at subsonic speeds and cooling by emitting bremsstrahlung. At roughly 10^7 cm above the surface the temperature begins to drop rapidly, with the cooling time becoming ever shorter as the temperature decreases. We refer to this region as the cooling zone. Eventually the temperature would drop to a point where the accretion column became optically thick and then level off at the temperature of the white dwarf's atmosphere. For
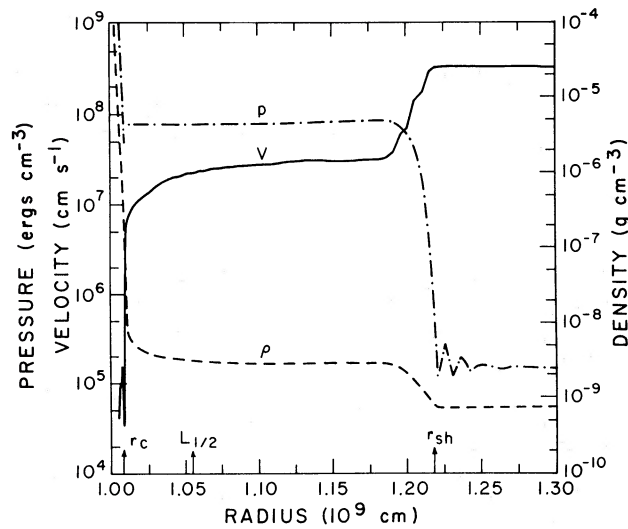
FIG. 1a
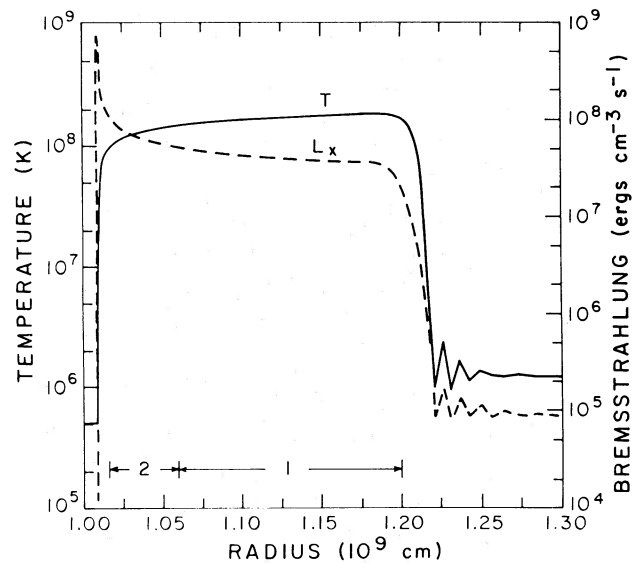
FIG. 1b
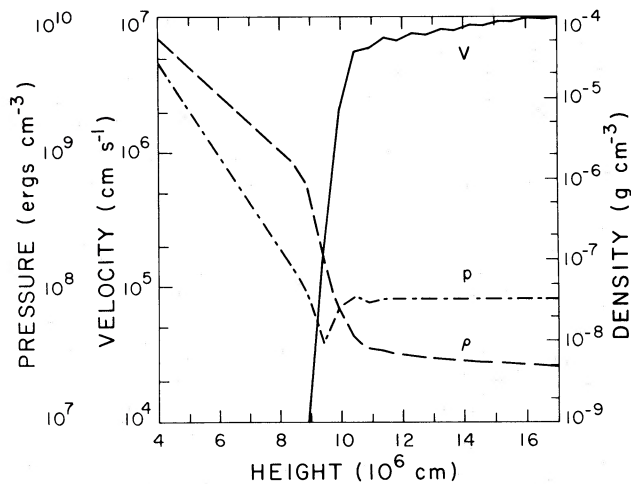
FIG. 1c
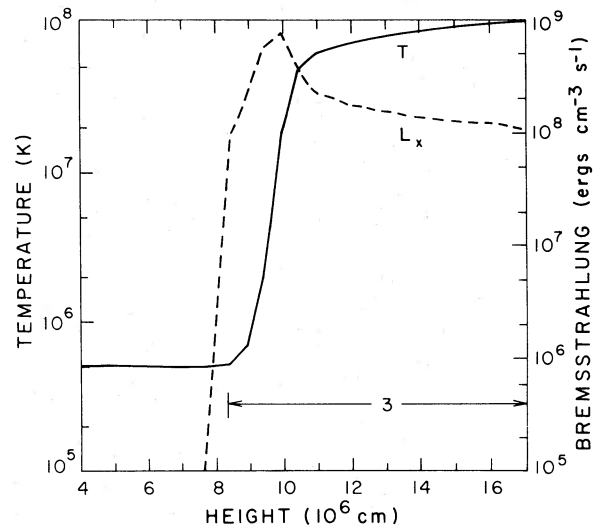
FIG. 1d

FIG. 1.—(a) The density, pressure, and magnitude of the velocity are shown as functions of radius for accretion onto a star with mass 0.5 $M_\odot$ and radius 10^9 cm. The accretion rate is 2.5×10^{15} g s^{-1} along a dipolar magnetic flux tube with area 10^{16} cm^2 at the surface of the star. These curves are shown for a time when the shock is moving upward and is at roughly half of its maximum height. The shock is at r_{sh} and the bottom of the cooling zone is at r_c. The pressure does not begin to increase until the flow has come nearly to a halt. Half of the luminosity is emitted above the point $L_{1/2}$. (b) The temperature and radiative losses as a function of radius. The regions marked (1) and (2) are used in calculating the cyclotron luminosity. (c) Same as Fig. 1a but with a smaller scale and centered on the cooling region. The dip in p is numerical noise. (d) Same as Fig. 1b. If the radiative cooling law had not been modified (see text), L_x would peak more sharply and then drop to zero.

numerical reasons, we have adjusted the radiative losses so that the cooling time never drops below t_{min}, which is chosen as ~0.1% of the oscillation period. The radiative cooling is set to zero below the surface temperature of the white dwarf. This has little effect on the solutions because the cooling zone is still very thin and the accretion luminosity is completely radiated away. Note that, due to this modification of the cooling law, the minimum value of r_{sh} has no physical meaning. Figure 1c shows that the velocity drops rapidly and the

density increases rapidly, in the cooling zone. The pressure, however, remains nearly constant throughout the cooling zone. The arrow labeled $L_{1/2}$ in Figure 1a shows the point in the flow above which half of the luminosity is emitted. In all of our solutions, this point is fairly close to the surface. Although the losses are greatest near the bottom of the cooling zone, the radiating volumes are such that most of the luminosity comes from the high-temperature regions.

These velocity, temperature, and density profiles are
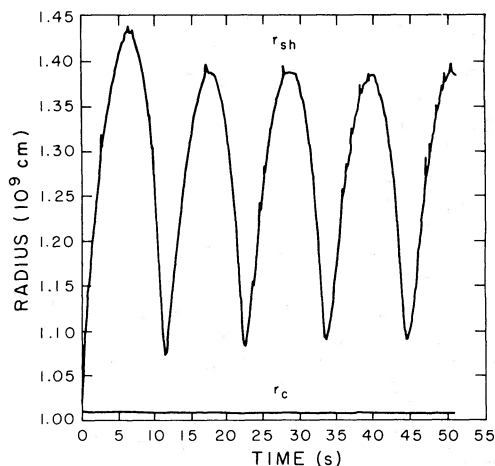
FIG. 2a
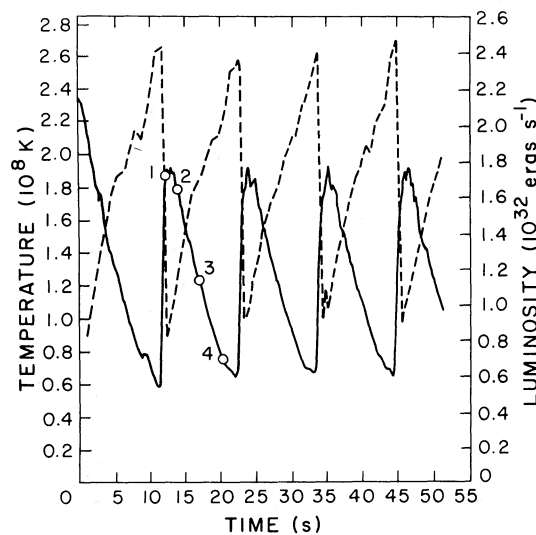
FIG. 2b

FIG. 2.—Properties of the shocked gas as a function of time for the same model as in Fig. 1: (a) the shock radius and the bottom of the cooling region; (b) the maximum temperature (*solid curve*) of the postshock gas and the bremsstrahlung luminosity (*dashed curve*). The numbers indicate the times for which spectra are shown in Fig. 5.

characteristic of most of our models. In particular, a region at nearly the postshock temperature followed by a narrow cooling zone is present in all of our models, although the temperatures and thicknesses vary.

In Paper I we showed that the accretion flow is unstable (see, e.g., Field 1965) and undergoes a periodic limit cycle when bremsstrahlung dominates the radiative losses. Figure 2 shows the postshock temperature, the distance between the shock and the base of the cooling zone, and the instantaneous luminosity as a function of time for the same model as in Figure 1. The temperature shows the same steep rise and slower decline found in Paper I. The shock height follows a curve with a period of 12.2 seconds and a cusp at minimum height. The luminosity has been smoothed slightly to remove numerical noise and exhibits a gentle rise, followed by a sharp drop. The same approximate shapes occur in all our models and are characteristic of the instability.

In Figure 3 we show the maximum shock height during an oscillation and the period of the oscillation as a function of the accretion rate (actually $\dot{M}/A_{cap}$) for $R = 10^9$ cm and $M = 0.5\ M_\odot$ and $1\ M_\odot$. The shock moves upward and the period increases as $\dot{M}/A_{cap}$ decreases because the lower postshock density leads to a longer radiative cooling time. For $\dot{M}/A_{cap} < 0.2$ g s^{-1} cm^{-2} and $M = 0.5\ M_\odot$ (and ~ 0.6 g s^{-1} cm^{-2} for $M = M_\odot$), there are no oscillatory solutions; the shock simply moves upward forever, or at least until the assumptions of our model break down. This phenomenon is discussed in more detail in § V. It occurs because the radiative cooling is never strong enough to let the accreting matter cool and settle onto the white dwarf.

In Figure 4 we show how the maximum shock height and the period of the oscillations depend on $\dot{M}/A_{cap}$ and the mass of the white dwarf. The radius of the white dwarf has been determined from the relation $R/5 \times 10^8$

cm $\approx M_\odot/M$ given by Hamada and Salpeter (1961). The shock height and the period both decrease as the mass of the white dwarf decreases. This happens because the lower gravitational potential leads to a lower postshock temperature and, therefore, a shorter cooling time. Figure 4 shows that the properties of the accretion flow
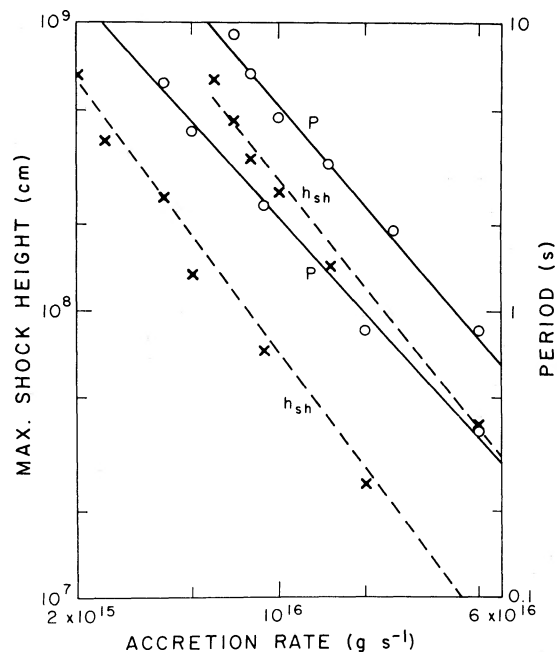
FIG. 3.—The dependence of the maximum shock height (*dashed curve*, ×) and the oscillation period (*solid curve*, ○) on the accretion rate. The white dwarf has a radius of 10^9 cm, and the polar cap area is 10^{16} cm^2 for both models. The curves toward the lower left are for a white dwarf with $M = 0.5\ M_\odot$; those toward the upper right are for $M = M_\odot$.
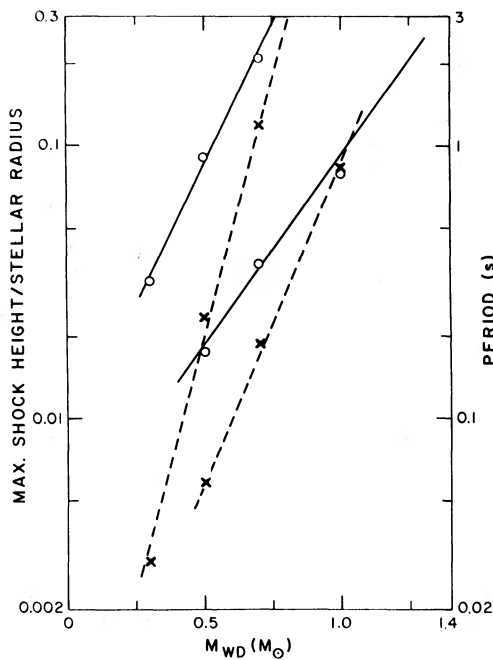
FIG. 4.—The dependence of the maximum shock height (*dashed curve*, ×) and the oscillation period (*solid curve*, ○) on the white dwarf mass for accretion rates of 2×10^{16} g s^{-1} (*right*) and 10^{17} g s^{-1} (*left*). The white dwarf radius is 5×10^{8} cm divided by its mass in units of the solar mass. The accretion column has an area of 10^{16} cm^{2}.

are strong functions of the white dwarf mass when $\dot{M}/A_{\rm cap}$ is held constant. This variation would be even more pronounced if we held the luminosity fixed as M was varied. The flow solutions obey a simple scaling law which is discussed in § V.

In Figure 5 we show the hard X-ray spectrum at several points in the cycle for the model used in Figure 1. The radiation is emitted at a range of temperatures and has an effective temperature significantly less than the peak temperature in the flow. As shown in the figure, a single-temperature thermal bremsstrahlung spectrum does not provide a good fit to the results. The basic difference is that the model spectra have additional emission at energies below ~10 keV. We note that observations of AM Her (Rothschild *et al.* 1981) have shown that the hard X-ray spectrum is not consistent with a single-temperature bremsstrahlung spectrum.

Our solutions are summarized in Table 1. The average properties of the flow are comparable to earlier steady state solutions (see, e.g., Wada *et al.* 1980). The shock height and oscillation period agree with the results presented in Paper I. However, our improved treatment of the radiative cooling prevents the buildup of material at temperatures ~10^{7} K (see Fig. 1 of Paper I) and yields a cusp, instead of a smooth curve, in the vicinity of the minimum shock height (see Figs. 2 of Paper I and this paper). This improvement has no effect on the conclusions of Paper I. The agreement between the two calculations also shows that the oscillation period and the maximum shock height are insensitive to the radiative cooling law at low temperatures.

FIG. 5.—The X-ray spectrum at four different times during the cycle (see Fig. 2b) for the model of Fig. 2. The dashed curves show single-temperature bremsstrahlung spectra for temperatures bracketing the range of peak temperatures found in the flow. The model spectra always have an excess of soft photons when compared to the spectra emitted at the hottest point in the flow.

TABLE 1

TIME-DEPENDENT SOLUTIONS[a]

$\dfrac{M}{M_\odot}$	$\dfrac{R}{10^9 \text{ cm}}$	$\dfrac{\dot{M}}{10^{16} \text{ g s}^{-1}}$	$\dfrac{h_{\rm sh}}{R}$	P[b]	$\left(\dfrac{P}{t_{\rm ff}}\right)$[c]	$(\Psi R_9 \phi^{-3/2})$[d]
0.3	1.67	2.0	0.0030	0.32	0.042	43.9
0.5	1	10.0	0.0059	0.174	0.063	28.2
0.5	1	5.0	0.0092	0.38	0.138	14.1
0.5	1	2.0	0.0235	0.91	0.33	5.66
0.5	1	0.885	0.073	2.33	0.85	2.50
0.5	1	0.5	0.133	4.22	1.54	1.41
0.5	1	0.4	0.25	6.2	2.26	1.13
0.5	1	0.25	0.39	11.0	4.01	0.71
0.5	1	0.2	0.66	18.6	6.77	0.57
0.7	0.71	10.0	0.019	0.37	0.27	7.25
0.7	0.71	2.0	0.12	2.1	1.5	1.45
1.0	1	5.0	0.040	0.86	0.44	5.00
1.0	1	2.5	0.09	1.9	0.98	2.50
1.0	1	1.5	0.15	3.25	1.67	1.50
1.0	1	1.0	0.26	4.7	2.42	1.00
1.0	1	0.8	0.34	6.7	3.45	0.80
1.0	1	0.7	0.46	9.1	4.69	0.70
1.0	1	0.6	0.64	12.2	6.28	0.60
1.0	0.5	10.0	0.084	0.79	1.15	1.77
1.0	0.5	8.0	0.13	0.95	1.38	1.41

[a] $A_{\rm cap} = 10^{16}$ cm^2.
[b] P is the period of the oscillation in seconds.
[c] $t_{\rm ff}$ is the free-fall time at the surface of the white dwarf.
[d] $\Psi = \dot{M}/A_{\rm cap}$ in cgs units and ϕ is the dimensionless gravitational potential (see eq. [1]).

V. DISCUSSION

In this section we provide physical explanations of our numerical results and quantify some of their properties. We show that the period of the limit cycle and the maximum shock height can be explained in terms of the radiative cooling time and a typical flow velocity. We discuss the source of the instability and show that its existence depends upon the form of the radiative cooling law. Finally, we discuss the conditions under which cyclotron emission can be ignored and present a simple scaling law for the period of the cycle and the maximum shock height.

a) Comparison with Simple Models

The gas crossing the shock must first cool off before it can settle onto the photosphere and leave the accretion column. The cooling time just behind the shock is (see eq. [11])

$$t_{br} = 1.1 \phi \Psi^{-1} \text{ s} , \tag{29}$$

where the postshock density of $4n_{ff}$ (eq. [5]) and temperature T_{sh} (eq. [6]) appropriate for a strong stationary shock have been inserted. In steady state, the shock height will be just high enough that the flow time to the surface is equal to the time required by the gas to cool to the photospheric temperature. Most of this distance is covered while the matter is still traveling at the postshock velocity. Thus, the equilibrium shock height is

$$h_{eq} \approx t_{br} V_{ff}/4 = 1.4 \times 10^8 \phi^{3/2} \Psi^{-1} \text{ cm} . \tag{30}$$

As an example we compare h_{eq} to the maximum shock height for $A_{cap} = 10^{16} \text{ cm}^2$ and $\phi = 1$. For $\dot{M}_{16}$ in the range from 0.6 to 5, h_{eq} lies in the range $(0.28-2.4) \times 10^8$ cm, while the maximum shock height (see Table 1) lies in the range $(0.4-6.4) \times 10^8$ cm. The two heights show the same dependence on $\dot{M}$, and the maximum shock height is, as expected, bigger than the approximate value for the equilibrium height.

The period of the cycle is the time required by the shock to travel from its minimum to its maximum height and back again. The shock velocity is 0 at maximum shock height and $V_{ff}/3$ (by the jump conditions) when the shock starts its upward motion. The period should be roughly $2h_{eq}$ divided by $V_{ff}/6$. This equals $3t_{br}$, which is in good agreement with the numerical result of $\sim 4t_{br}$ (see Table 1). This discussion has explained the magnitudes of the limit cycle period and the maximum shock height, and how they depend on the accretion rate and the properties of the white dwarf.

Previous papers on these systems have generally solved the time-independent hydrodynamic equations to obtain the equilibrium flow solution. This does not, of course, guarantee that such a solution is stable. We would now like to present a simple model that checks for the stability of the equilibrium solution. As a first step we note that the strong shock jump conditions, when modified to account for a nonzero velocity V_s, are

$$V = (-V_{ff} + 3V_s)/4 ,$$
$$T = 3\mu(V_{ff} + V_s)^2/(16k_B) . \tag{31}$$

The density increases by a factor of 4. In some situations, bremsstrahlung will not be the dominant radiative cooling process. To account for this possibility we multiply the radiative losses by a factor of $(T/T_*)^{\alpha - 1/2}$ (see eq. [28] for T_*) so that the cooling is proportional to $n^2 T^\alpha$. When the modified cooling law and the new jump conditions are employed, the estimate for the cooling length (which need not be the same as the shock height) is

$$h = h_{eq}(1 - 3V_s/V_{ff})(1 + V_s/V_{ff})^{2-2\alpha} . \tag{32}$$

We now consider perturbations where a shock at h_{eq} is given a small velocity V_s. The perturbation changes the postshock velocity and cooling time so that the flow requires a different distance to cool and come to a halt. If $h > h_{eq}$, the material crossing the shock will not cool off before reaching the photosphere. The resulting accumulation of matter behind the shock produces an excess pressure which acts to force the shock upward. If $h < h_{eq}$, the shock is forced downward due to a lowered postshock pressure. If the flow is to be stable, $h > h_{eq}$ must hold when $V_s < 0$ (a downward velocity), and vice versa. An analysis of equation (32) shows that the solutions are stable only if $\alpha > -\frac{1}{2}$.

This model is very approximate, so it is not surprising that the numerical models indicate that stability occurs only for $\alpha \gtrsim 1.6$ (see Paper I; note that $\alpha = 1.1$ there is the same as $\alpha = 1.6$ in the present paper). The main point to recognize is that the steady state solution requires a balance between the amount of material crossing the shock and the amount cooling and settling onto the photosphere. When a perturbation is made, the rates for both processes change. Stability requires that the response to a downward perturbation of the shock must be that matter crosses the shock faster than it cools off. This results in an excess pressure which pushes the shock back up to its equilibrium position. The importance of the dependence on α is that other radiative processes, e.g., cyclotron emission, have a different dependence on temperature than bremsstrahlung. Most radiative cooling processes do not have a simple $n^2 T^\alpha$ dependence. However, we have shown that, if this form can be made to fit across the relevant temperature range, the cooling law must be roughly one power of T steeper than bremsstrahlung to achieve stability.

b) Minimum $\dot{M}$

An interesting feature of the results presented in § IV (where $M = 0.5 M_\odot$, $R = 10^9$ cm, $A_{cap} = 10^{16}$ cm^2) is that, for $\dot{M} \lesssim 2 \times 10^{15}$ g s^{-1}, the shock radius r_{sh} moves steadily outwards as time increases. We will now attempt to gain some insight into this phenomenon from a qualitative analysis of the steady state shock.

If we generalize equation (30) for the steady state shock height to include the variation of A, n, T, and V_{ff} with radial distance, we find that

$$r_{sh} - R = \frac{3V_{ff}^2(R)}{16n_{ff}(R)C_{br}} \left(\tfrac{3}{16}\mu k_B\right)^{1/2} \left(\frac{r_{sh}}{R}\right)^{s-3/2} \tag{33}$$

(see eq. [11] for C_{br}).

If we set $y = r_{sh}/R$, the shock height, in units of R, is given by the roots $(y > 1)$ of the equation,

$$f(y) \equiv \beta y^{s-3/2} - y + 1 = 0, \qquad (34)$$

where

$$\beta = 0.14\phi^{3/2}\Psi^{-1}. \qquad (35)$$

Since $\beta > 0$, we note that $f(1) > 0$. The function $f(y)$ is plotted for several values of s and β in Figure 6. For $s < 5/2$, we find that there is always a unique root of $f(y)$. For $s = 5/2$, there is a unique root if $\beta < 1$. For $s > 5/2$, we find that there are two roots if

$$\beta < \beta_c = (s - 3/2)^{-1}[1 - 1/(s - 3/2)]^{s-5/2} < 1, \qquad (36)$$

and no roots if $\beta > \beta_c$. For the case $s = 3$, this requires $\beta < 2/[3(3)^{1/2}]$. This predicts that there is no standing shock if $\dot{M} < 1.3 \times 10^{15}(A_{cap}/10^{16} \text{ cm}^2) \text{ g s}^{-1}$ for $M = 0.5 \, M_\odot$, $R = 10^9$ cm (the numerical solution gives $\dot{M} \lesssim 2 \times 10^{15} \text{ g s}^{-1}$). The reason for this behavior is that the rapid increase in the area, combined with a constant mass flux, leads to a rapidly decreasing post-shock density when the shock moves more than $\sim R/2$ above the surface. The resulting increase in the cooling time is so rapid that, even accounting for the increasing flow distance, the gas never has time to cool before reaching the surface. If $\beta < 2/[3(3)^{1/2}]$, one root occurs for $y < 3$ and the other for $y > 3$. The latter root is
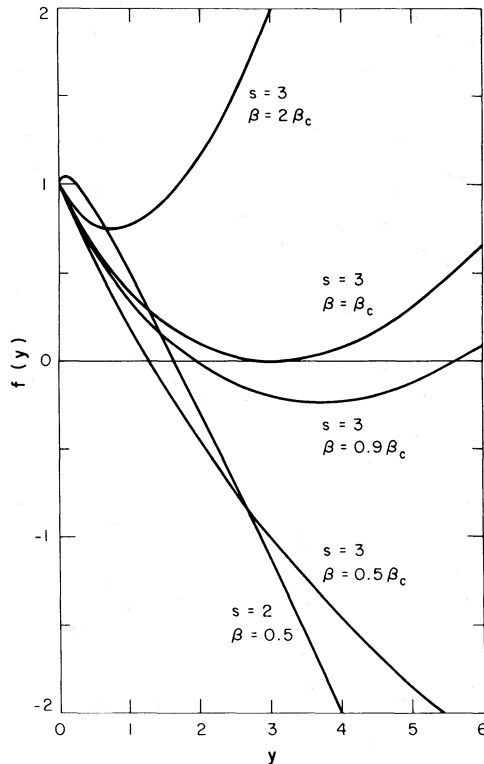
unphysical since the assumptions of constant physical parameters in the postshock region breaks down. These results can easily be extended to arbitrary values of M, R, and A_{cap} (see eq. [34]).

The above analysis assumes that the cooling is due to bremsstrahlung radiation. If cyclotron cooling is important, it is possible that a steady state shock could form for low $\dot{M}$ and large magnetic fields (see Langer and Rappaport 1982). The simple model also suggests that for radial accretion $(s = 2)$ an equilibrium shock height can be found, no matter how small $\dot{M}$ becomes.

c) Cyclotron Emission

We have ignored cyclotron emission in computing our solutions. We now estimate the conditions for which the neglect of this emission is justified. We divide the postshock region into three zones, each of roughly constant density and temperature, and assume the magnetic field is uniform throughout the postshock region. We then estimate the cyclotron radiation from each zone, ignoring absorption in zones above it, and using the angle-averaged cyclotron absorption coefficient. The cyclotron radiation would then be self-absorbed, following a Rayleigh-Jeans curve, up to a frequency $\omega^* = m^*\omega_c$, with negligible emission for $\omega > \omega^*$. If we use the fit for m_* given in equation (14), we find (see Table 2) that m^* is highest in zone 1 and decreases in zones 2 and 3. Here, zone 1 is at nearly the postshock temperature, while zones 2 and 3 are farther down in the cooling zone (see Figs. 1b and 1d). This shows that the principal cyclotron emission comes from the top (hottest) zone. This zone would also absorb the cyclotron emission from the zones below it. The value of m^* is slightly larger for the lower accretion rate because of its greater shock height. The cyclotron radiation for both models peaks at optical wavelengths when $B = 10^7$ gauss. The cyclotron luminosity is less than the accretion luminosity if the magnetic field is small enough. For a white dwarf with a mass $M = 0.5 \, M_\odot$ and a radius of 10^9 cm, we require $B < 1.4 \times 10^7$ gauss when $\dot{M} = 2.5 \times 10^{15} \text{ g s}^{-1}$, and $B < 3.4 \times 10^7$ gauss when $\dot{M} = 2 \times 10^{16} \text{ g s}^{-1}$, to ensure that cyclotron emission is unimportant. This shows that our models, which include only bremsstrahlung emission, are accurate for $B \lesssim 10^7$ gauss.

d) The Scaling Law

We have found that our results obey a simple scaling law. Figure 7 shows the maximum shock height (in units of the stellar radius) and the limit cycle period (in units of the free-fall time) as a function of the scaling parameter, $\Psi R_9 \phi^{-3/2}$. The scaling law can be roughly approximated by (see Fig. 7)

$$\frac{10(r_{sh} - r_c)}{R} \approx \frac{P}{t_{ff}} \approx \frac{2}{\Psi R_9 \phi^{-3/2}}, \qquad (37)$$

where P is the oscillation period and the bottom of the cooling zone lies at r_c. This shows that

$$P \propto (M/R)(A_{cap}/\dot{M}). \qquad (38)$$

FIG. 6.—Plot of $f(y)$ vs. y for various values of β and s. The roots of $f(y) = 0$ give the shock height in units of the stellar radius for the simple static model. For $s > 5/2$ there are two roots for $\beta < \beta_c$ and no roots for $\beta > \beta_c$.

TABLE 2

Self-absorbed Cyclotron Radiation in the Shock-heated Region[a]

Accretion Rate (g s^{-1})	Zone[b]	Thickness (cm)	Electron Number Density (cm^{-3})	T (K)	m^{*} [c]	$(\lambda^* B_7)$[d] (Å)	$\left(\dfrac{L_{\mathrm{cyc}} B_7^{-3}}{L}\right)$[e]
2.5×10^{15}	1	1.5×10^8	1.2×10^{15}	1.7×10^8	14.5	7390	0.34
	2	3.9×10^7	2.4×10^{15}	1.1×10^8	11.3	9480	0.074
	3	8.5×10^6	4.5×10^{15}	6.0×10^7	8.0	13,400	0.014
2×10^{16}	1	1.1×10^7	1.5×10^{16}	1.7×10^8	14.4	7440	0.026
	2	3.1×10^6	2.3×10^{16}	1.1×10^8	11.1	9650	0.008
	3	1.9×10^6	3.5×10^{16}	6.5×10^7	8.5	12,600	0.002

[a] The cross sectional area of the column $= 10^{16}$ cm^2 at the surface of the white dwarf of mass $M = 0.5\, M_\odot$, $R = 10^9$ cm.

[b] Zones of roughly constant density and temperature. Zone 1 is just below the shock front. Zones 2 and 3 are below that. See Fig. 1.

[c] Cyclotron radiation is self-absorbed up to a frequency $m^*\omega_c$ where m^* is from the fit to the results of Chanmugam and Wagner 1979 found by Wada et al. 1980.

[d] $\lambda^* = 2\pi c/m^*\omega_c$ is the peak wavelength for the cyclotron radiation. B_7 = magnetic field in units of 10^7 gauss.

[e] L_{cyc}/L = ratio of cyclotron luminosity to accretion luminosity.

e) The Minimum Shock Height

The shock moves upward when there is more gas crossing the shock than gas cooling to the photospheric temperature, and it moves downward when the opposite relation holds. This response must occur to preserve an approximate balance between the ram pressure of the accreting gas and the thermal pressure of the postshock gas. When the shock is moving downward ($V_s < 0$), the postshock temperature is less than when $V_s > 0$ (see eq.
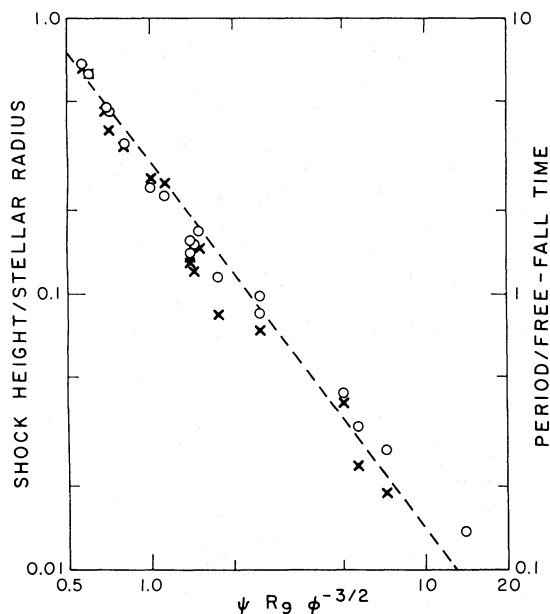
FIG. 7.—The shock height in units of the white dwarf radius and the period in units of the free-fall time as functions of the dimensionless scaling parameter (see text). The results for different white dwarf masses and radii cluster along a single curve. The scatter in the points is mostly due to numerical uncertainty.

[31]). The lower temperature allows the gas to cool more rapidly and thus enhances the downward motion of the shock. Our solutions show that the downward motion is so rapid that the postshock Mach number reaches ~ 0.8 and significant pressure gradients develop. This is in sharp contrast to the situation for $V_s > 0$ when the Mach number is ~ 0.1, allowing sound waves to equalize the pressure between the shock and the photosphere (see Fig. 1). The downward motion of the shock continues until the reservoir of hot gas built up while $V_s > 0$ is depleted. The gas at the photospheric temperature is optically thick and does not cool efficiently. It is this cutoff in the cooling that causes a halt to the downward motion of the shock (the ram pressure is not great enough for the shock to enter the photosphere). Because the photosphere does not move, any gas crossing the shock after the minimum height is reached must have zero flow velocity. The jump equations (31) show that the shock must then begin to move upward with a velocity of $V_{\mathrm{ff}}/3$. This rapid change of V_s explains the cusp at minimum shock height in Figure 2a. An interesting point to note is that when the shock is moving upward and crosses the equilibrium height the postshock temperature is too high to allow the gas to cool before reaching the surface. The shock thus continues upward until the gas does have enough time to cool, and then stops. The gas then has the same postshock temperature as the equilibrium solution, but the shock is too high. When the shock reaches the equilibrium height with $V_s < 0$, the postshock temperature is lower, so the gas is cooling too rapidly and the shock continues downward. As a result, the shock continues to move up and down, instead of stopping at the equilibrium height.

Our numerical model finds a solution on a gird of points which is too coarse to resolve fully the flow structure that would occur in a real accretion column

near minimum shock height. In addition we do not properly treat the transition to optically thick radiative cooling. As a result, our model does not obtain an accurate solution to the flow for a short time interval around the minimum shock height. However, the details of the flow are irrelevant because the shock must quickly start to move upward at a velocity $V_{ff}/3$ after getting very close to the photosphere, and the numerical model reproduces this behavior. In Paper I we used a different treatment of the radiative cooling and found a different behavior near minimum shock height. However, the limit cycle period and the maximum shock height obtained in Paper I are the same as in the current work, demonstrating the insensitivity of the results to the treatment of the flow near minimum shock height.

Our model cannot determine exactly how close the shock comes to the photosphere. It is even possible that the flow might become nonhydrodynamic with the accretion energy being deposited within a mean free path of the accreting ions. However, such a condition cannot persist for long because the amount of material within a Coulomb stopping length is incapable of radiating away the accretion luminosity, unless the accretion rate is extremely small. The material in the stopping region would rapidly heat up, and the interface where thermalization occurs (over a mean free path) would move up the column. Such an interface is commonly known as a shock. The flow thus rapidly reverts to being hydrodynamic, and our model once again applies. The details of the flow during this short time interval do not influence the rest of the cycle and may safely be ignored.

Heat conductivity should become important whenever there are large temperature gradients. The largest temperature gradients occur when the shock is at its minimum height. Heat conduction will act to prevent excessively steep temperature gradients and might serve to determine the minimum shock height. Because of our numerical treatment of the radiative cooling we cannot answer this question. However, heat conductivity cannot prevent the upward motion of the shock which serves to reduce the temperature gradients and hence the heat flux. In a short time, the shock is high enough that our numerical results apply, and heat conduction is then unimportant for the rest of the cycle.

In summary, we have shown that the precise behavior of the flow at minimum shock height has no influence on the rest of the cycle. This short time interval should have no observable consequences, so we have chosen a numerically convenient treatment which preserves the overall behavior, in spite of its failure to provide the precise radial dependence of the temperature, velocity, etc., during this short time interval.

VI. CONCLUSIONS

In this paper we have considered one-dimensional, time-dependent accretion onto magnetized white dwarfs, where the principal cooling mechanism is optically thin bremsstrahlung. We have found:

1. The flow is thermally unstable and the height of the shock undergoes periodic oscillations. For white dwarfs with masses in the range from 0.5 to 1 $M_\odot$, the periods range from a fraction of a second to ~ 10 s, depending on the accretion rate per unit area. We have also shown that if some process other than bremsstrahlung dominates the cooling, the flow may be stable.

2. For accretion rates below a certain critical value, which depends on the properties of the white dwarf, the solution changes character and the shock moves upward indefinitely. At approximately the same $\dot{M}$, the steady state equations cease to have a solution.

3. The flow solution depends on a single dimensionless parameter which in turn is a function of the mass and radius of the white dwarf and the accretion rate per unit area.

The observed luminosities in the different energy bands provide a way to determine the basic properties of the accretion flow without recourse to a detailed model of the accretion column. Quantities that can be determined include the accretion rate, the area of the accretion column, the density of the postshock gas, and the volume of the hard X-ray–emitting region. These values set the range of accretion rates and accretion column areas which theories must consider and provide a consistency check on the predictions of the resulting model. However, caution must be used in attempting to deduce the parameters of the flow from the observations because no observations have been made in the extreme ultraviolet at the peak of the blackbody flux. As a result, the quoted values for the blackbody temperature and luminosity may be in error. Thus, *observations of the AM Her stars in the extreme-ultraviolet would be extremely helpful in determining the properties of the accretion column.*

In making the calculations presented in this paper, we have considered system parameters which are not directly relevant to the AM Her stars. For other conditions, processes such as cyclotron emission, heat conduction, and nuclear burning on the surface of the white dwarf can significantly affect the predicted spectrum and other results. These questions will be dealt with in subsequent papers.

X-ray and optical pulsations can provide useful comparisons between observations and theory. The AM Her stars have been observed to flicker (Panek 1980; Bond, Chanmugam, and Grauer 1979) on time scales longer than 30 seconds. Our model predicts periods significantly shorter than this for which few observations are available. We note that, if the accretion rate per unit area is not uniform across the accretion column, there should be a range of oscillation periods. In addition, different flux tubes may oscillate independently with random relative phases. As a result, we expect that the radiation will exhibit short-term variability with periods corresponding to the mean accretion rate per unit area. We also note that the luminosity of the AM Her systems can vary by 50% on a time scale of 100 seconds (see, e.g., Panek 1980). This shows that the oscillations will be disrupted by large amplitude perturbations every 10–1000 cycles. Thus, there might be no way to tell observationally if the oscillations are damped, provided $Q \gtrsim 100$. The recent results reported by Middleditch

(1982) suggest that this type of instability, with a characteristic period of the order of 1.7 s, is present in the systems An UMa and E1405-451. Further observations of variability on roughly this time scale are clearly of great interest.

APPENDIX A

THE DIFFERENCE EQUATIONS

The flow equations (25) are solved numerically by an implicit finite difference method on an Eulerian grid of points r_i. There are N zones of width Δr_i centered at the points r_i [by definition $r_{i+1} = r_i + \frac{1}{2}(\Delta r_i + \Delta r_{i+1})$]. Thus, the lower boundary of our system is at $r_1 - \Delta r_1/2$ and the upper boundary is at $r_N + \Delta r_N/2$. As a boundary condition at r_N we specify E_N, k_N, and m_N in terms of the accretion rate $\dot{M}$, an initial temperature, and the velocity (generally we assume free fall, $V_N = (2GM/r_N)^{1/2}$). We place the lower boundary well inside the nearly hydrostatic portion of the stellar atmosphere where the pressure is much greater than the ram pressure of the accreting gas. As a result, the solution does not depend on the exact form of the boundary condition, which we have taken as zero mass flux through the lower boundary at $r_1 - \Delta r_1/2$ (i.e., $k_{1/2} \equiv 0$). This avoids the use of a rigid lower boundary at a point where this would influence the solution.

The following form has been adopted for the mass difference equation

$$\frac{m_i^{n+1} - m_i^n}{\Delta t} = -\left(\frac{k_{i+1/2}^{n+1} - k_{i-1/2}^{n+1}}{\Delta r_i}\right), \qquad k_{i+1/2}^{n+1} \equiv \frac{k_{i+1}^{n+1} + k_i^{n+1}}{2}, \tag{A1}$$

where i designates a radius, and n, a time. This equation is implicit and conserves mass, as can be seen from the following calculation

$$\Delta m \equiv \sum_{i=1}^{N} \Delta r_i (m_i^{n+1} - m_i^n) = -\Delta t \sum_{i=1}^{N-1} (k_{i+1/2}^{n+1} - k_{i-1/2}^{n+1}) + (m_N^{n+1} - m_N^n)\Delta r_N = -\Delta t\, k_{N-1/2}^{n+1} = \Delta t\, \dot{M}_{N-1/2}. \tag{A2}$$

The boundary conditions that there is no flow through the lower boundary ($k_{1/2} \equiv 0$) and that the upper boundary is static ($m_N^{n+1} \equiv m_N^n$) have been used in simplifying this expression. The result is that the change in mass is the mass flux at the lower boundary of the top zone, $-k_{N-1/2}$, times the time step Δt. The ability to ensure *numerical* conservation of mass was one reason for placing boundary conditions at $r_1 - \frac{1}{2}\Delta r_1$, not at r_1.

The chosen form for the energy difference equation is

$$\frac{E_i^{n+1} - E_i^n}{\Delta t} = -\frac{1}{\Delta r_i}\left\{(JA)_{i+1/2}^{n+1} - (JA)_{i-1/2}^{n+1} + \left[\frac{k}{m}(E + pA - \sigma A)\right]_{i+1/2}^{n+1}\right.$$

$$\left. - \left[\frac{k}{m}(E + pA - \sigma A)\right]_{i-1/2}^{n+1}\right\} - \left(\frac{m^2}{4\mu^2 A}\epsilon_{\text{rad}}\right)_i^{n+1}, \tag{A3}$$

where

$$\left[\frac{k}{m}(E + pA - \sigma A)\right]_{i+1/2}^{n+1} \equiv \frac{k_{i+1/2}^{n+1}}{m_{i+1/2}^{n+1}}\left[E_{i+1/2}^{n+1} + (pA - \sigma A)_{i+1/2}^{n+1}\right]. \tag{A4}$$

All quantities at $i + 1/2$ are evaluated as in equation (A1).

Equation (25) is equivalent to:

$$\frac{\partial k}{\partial t} = -\frac{k}{m}\frac{\partial k}{\partial r} + m\frac{\partial}{\partial r}\left(\frac{GM}{r} - \frac{1}{2}\frac{k^2}{m^2}\right) - \frac{\partial}{\partial r}[(p - \sigma)A] + \frac{s}{r}(p - \sigma)A, \tag{A5}$$

where

$$pA = \frac{2}{3}\left(E + \frac{GM}{r}m - \frac{1}{2}\frac{k^2}{m^2}\right). \tag{A6}$$

We write the difference equation as

$$\frac{k_i^{n+1} - k_i^n}{\Delta t} = \frac{1}{2}\left[\left(\frac{\partial k}{\partial t}\right)_{i+1/2}^{n+1} + \left(\frac{\partial k}{\partial t}\right)_{i-1/2}^{n+1}\right],$$ (A7)

where

$$\left(\frac{\partial k}{\partial t}\right)_{i+1/2}^{n+1} = -\frac{(k_{i+1} + k_i)(k_{i+1} - k_i)}{(m_{i+1} + m_i)(r_{i+1} - r_i)} + \frac{(m_i + m_{i+1})}{2(r_{i+1} - r_i)}\left(\frac{GM}{r_{i+1}} - \frac{GM}{r_i} - \frac{1}{2}\frac{k_{i+1}^2}{m_{i+1}^2} + \frac{1}{2}\frac{k_i^2}{m_i^2}\right)$$
$$-\frac{[(p - \sigma)A]_{i+1} - [(p - \sigma)A]_i}{r_{i+1} - r_i} + s\frac{\{[(p - \sigma)A]_{i+1} + [(p - \sigma)A]_i\}}{(r_i + r_{i+1})},$$ (A8)

and all quantities on the right-hand side are evaluated at time t_{n+1}. Note that when the Lagrangian derivative $[(\partial k/\partial t) + (k/m)(\partial k/\partial r)]$ and $(p - \sigma)$ are zero, the difference equation is satisfied by the exact free-fall solution $k^2/m^2 = 2GM/r$. This equation also admits a simple recursive solution for a hydrostatic, isothermal atmosphere:

$$m_{i+1} = \left\{1 + \left[\frac{2k_B Ts}{\mu(r_{i+1} + r_i)} - \frac{GM}{r_{i+1}r_i}\right]\left[\frac{1}{2}\frac{GM}{r_{i+1}r_i} + \frac{k_B T}{\mu}\left(\frac{1}{r_{i+1} - r_i} - \frac{s}{r_{i+1} + r_i}\right)\right]^{-1}\right\}m_i.$$ (A9)

This solution eliminates the need to wait for the dense, nearly static portions of the atmosphere to relax when a model is started up. The energy and momentum equations (eqs. [A3] and [A7]) have both been written so that the term at $i - \frac{1}{2}$ is zero for $i = 1$ (except for the heat flux) by the boundary condition of no mass flux through the bottom $(k_{1/2} \equiv 0)$. Because of the presence of gravity, the momentum equation cannot be written in a conservative form.

As written, these equations are nonlinear in the future solution. We treat this by linearizing in the future solution. For example, we write

$$\frac{(k_i^{n+1})^2}{m_i^{n+1}} \to 2\frac{k_i^n}{m_i^n}k_i^{n+1} - \left(\frac{k_i^n}{m_i^n}\right)^2 m_i^{n+1}.$$ (A10)

In practice we have found that, with time steps chosen so that the solution does not change greatly between time t_n and t_{n+1}, this linearization accurately approximates the implicit system.

It is convenient to express the equations (25) in matrix form. Let

$$U_i^n \equiv \begin{pmatrix} m \\ k \\ E \end{pmatrix}_i^n.$$ (A11)

Then equations (25) can be reduced to the form:

$$\tilde{A}_i U_{i+1}^{n+1} - \tilde{B}_i U_i^{n+1} + \tilde{C}_i U_{i-1}^{n+1} = U_i^n + \tilde{S}_i^n,$$ (A12)

where $\tilde{A}_i$, $\tilde{B}_i$, and $\tilde{C}_i$ are 3 × 3 matrices which depend on conditions at the "present" time (corresponding to superscript n). The right-hand side contains the present solution and a source term S_i^n which does not involve any "future" variables. We next make the *Ansatz*

$$U_i^{n+1} = \tilde{E}_{i+1}U_{i+1}^{n+1} + \tilde{F}_{i+1}^{n+1},$$ (A13)

where $\tilde{E}_{i+1}$ is a 3 × 3 matrix, $\tilde{F}_{i+1}$ is a 3 × 1 matrix, and both sets of matrices $\tilde{E}_{i+1}$ and $\tilde{F}_{i+1}$ are as yet undetermined. This may be substituted into equation (A12) to obtain

$$U_i^{n+1} = (\tilde{C}_i\tilde{E}_i - \tilde{B}_i)^{-1}(U_i^n - \tilde{C}_i\tilde{F}_i - \tilde{A}_i U_{i+1}^{n+1} + \tilde{S}_i^n).$$ (A14)

A comparison of equations (A13) and (A14) shows that

$$\tilde{E}_{i+1} = (\tilde{B}_i - \tilde{C}_i\tilde{E}_i)^{-1}\tilde{A}_i,$$ (A15)

while

$$\tilde{F}_{i+1} = -(\tilde{B}_i - \tilde{C}_i\tilde{E}_i)^{-1}(U_i^n - \tilde{C}_i\tilde{F}_i + \tilde{S}_i^n).$$ (A16)

An iterative solution for $\tilde{E}_i$ and $\tilde{F}_i$ may then be obtained with the use of the boundary conditions. The future solution U_i^{n+1} can then be obtained by back substitution in equation (A13).

To deal with the numerical instabilities induced by the discontinuity at the shock and the large temperature gradient at the base of the cooling zone, we have introduced artificial dissipation into the flow equations. This includes

artificial viscosity and heat conductivity and the use of a Shuman filter (Harten and Zwas 1972). The stress due to artificial viscosity is

$$\sigma_i = -\tfrac{4}{3}f_{\mathrm{vis}}\frac{m_i}{A_i}\left(\frac{k_{i+1/2}}{m_{i+1/2}} - \frac{k_{i-1/2}}{m_{i-1/2}}\right)^2 \tag{A17}$$

for $\partial V/\partial r < 0$, and zero for $\partial V/\partial r > 0$. Thus, there is a nonzero viscous stress only when the fluid is undergoing compression ($\partial V/\partial r < 0$). The dimensionless constant f_{vis} is employed to control the strength of the viscosity. The chosen form means that viscosity acts in regions where large absolute changes in the velocity occur. In practice, the artificial viscosity spreads the shock across several zones of the numerical mesh and has little effect elsewhere. For purposes of comparison, the stress due to real viscosity is

$$\sigma_{\mathrm{real}} = \tfrac{4}{3}\mu_{\mathrm{vis}}\frac{\partial}{\partial r}\frac{k}{m}, \tag{A18}$$

where μ_{vis} is a constant depending on the temperature (see eq. [24]). This stress is small enough that it has no effect on the solution and thus has not been included in the equations.

The energy flux due to heat conduction is

$$J = -K\frac{\partial T}{\partial r}, \tag{A19}$$

where $T = pA/(\mu k_{\mathrm{B}} m)$. We include the real heat conduction (see eq. [21]), but it has little effect for the models presented in this paper. The following form has been chosen for the artificial heat conductivity:

$$K_i = f_{\mathrm{cond}}\frac{m_i}{A_i}\left|\frac{T_{i+1} - T_i}{T_{i+1} + T_i}\right|, \tag{A20}$$

where f_{cond} is a constant that can be adjusted to achieve the desired heat flux. This heat conduction is important wherever there are large fractional changes in the temperature. In practice, this occurs across the shock and at the base of the cooling zone. We have chosen f_{cond} so that its value in the cooling region is 40% of its value across the shock.

After each time step we apply a series of filters to the solution to smooth out rapid variations. We construct Shuman filters (see Harten and Zwas 1972) which remove components in the solution whose wavelength is close to the mesh spacing. The mesh is not capable of resolving variations on this small a distance scale so the filter does not throw away any real information, and the smoothing prevents instabilities due to inaccurate numerical estimates of derivatives (see Appendix B).

APPENDIX B

THE SHUMAN FILTER

The filter equation we employ (see Harten and Zwas 1972) is of the form

$$\tilde{X}_i = X_i + \theta_{i+1/2}(X_{i+1} - X_i) - \theta_{i-1/2}(X_i - X_{i-1}), \tag{B1}$$

where $\tilde{X}_i$ is the new (filtered) value for the variable X_i. This form of the filter has the property that it preserves the sum of X, i.e.,

$$\sum_{i=1}^{N-1}\tilde{X}_i = \sum_{i=1}^{N-1}X_i, \tag{B2}$$

provided $\theta_{1/2} = \theta_{N-(1/2)} = 0$. This property allows us to ensure the numerical conservation of mass established in the difference equation by filtering only the quantity $m_i\Delta r_i$. We first employ a filter designed to smooth out small deviations from free fall in the region above the shock. Next we filter out relative maxima and minima in the density, velocity, and temperature which are only one zone wide, and therefore below the resolution of the mesh. The remaining task is to choose the quantities to be filtered and the values of the filter constant θ. We have been guided in this choice by the types of instabilities which have occurred in our numerical models.

The first filter we employ is designed to remove small variations away from free fall in the highly supersonic flow above the shock. The filter constant has been chosen as

$$\theta_{i+1/2} = f_m\left(\frac{k_{i+1}^2}{m_{i+1}} - \frac{k_i^2}{m_i}\right)\frac{1}{(mV_{\mathrm{ff}}^2)_{i+1} + (mV_{\mathrm{ff}}^2)_i}, \tag{B3}$$

where f_m is an adjustable constant controlling the strength of the filter and $V_{\rm ff}$ is the free-fall velocity. This filter is adjusted by setting $\theta_{i+1/2}$ to zero at any point where $\theta_{i+1/2} < 2 \times 10^{-3} f_m$ or if

$$(\Delta r_{i+1} m_{i+1} - \Delta r_i m_i)(m_{i+1} - m_i) < 0 . \tag{B4}$$

The second condition prevents filtering when the mesh spacing is varying more rapidly than the density, so that filtering would act to increase undesired variations.

We apply this filter to the density by setting X_i to $m_i \Delta r_i$ in equation (B1). The new density, $\tilde{m}_i$, is smooth in the free-fall region, and the total mass has been conserved in the process because $\theta_{1/2}$ and $\theta_{N-1/2}$ were set to zero. It should be noted that the filter is never applied at the point r_N because the boundary condition fixes the solution at that point. We next apply the same filter to the sum of the kinetic and thermal energy (the gravitational potential energy is smooth due to the previous filter). The filter equation is

$$\tilde{E}_i \Delta r_i = E_i \Delta r_i + \theta_{i+1/2} \left[\Delta r_{i+1} \left(E_{i+1} + \frac{GM}{r_{i+1}} \tilde{m}_{i+1} \right) - \Delta r_i \left(E_i + \frac{GM}{r_i} \tilde{m}_i \right) \right]$$

$$- \theta_{i-1/2} \left[\Delta r_i \left(E_i + \frac{GM}{r_i} \tilde{m}_i \right) - \Delta r_{i-1} \left(E_{i-1} + \frac{GM}{r_{i-1}} \tilde{m}_{i-1} \right) \right] . \tag{B5}$$

This filter conserves the total energy and does not redistribute gravitational potential energy.

We next compute the velocity and temperature,

$$V_i = \frac{k_i}{\tilde{m}_i}, \qquad T_i = \frac{2}{3} \frac{\mu}{k_{\rm B}} \left(\frac{\tilde{E}_i}{\tilde{m}_i} + \frac{GM}{r_i} - \frac{1}{2} \frac{k_i^2}{\tilde{m}_i^2} \right) \tag{B6}$$

and apply a second group of filters. These filters are designed to smooth out the density, temperature, and velocity at points where they have relative maxima or minima that are only one zone wide (the mesh is not fine enough for the solution to contain any information on that scale). This may be accomplished by setting $\theta_{i+1/2}$ and $\theta_{i-1/2}$ to a constant f_w if

$$(X_{i+1} - X_i)(X_i - X_{i-1}) < 0 , \tag{B7}$$

and otherwise setting them to zero. The constant f_w lies between 0 and 1 and is chosen to give the desired level of filtering. This filter is applied to V_i and T_i, to produce filtered quantities $\tilde{V}_i$ and $\tilde{T}_i$. A similar filter is applied to $\Delta r_i \tilde{m}_i$ to set $\Delta r_i \tilde{\tilde{m}}_i$, but the previously determined $\theta_{i+1/2}$ is set to 0 for any point satisfying equation (B4). These filtered quantities are then used to set a filtered solution:

$$m_i \leftarrow \tilde{\tilde{m}}_i , \qquad k_i \leftarrow \tilde{\tilde{m}}_i \tilde{V}_i ,$$

and

$$E_i \leftarrow \tfrac{1}{2} \tilde{\tilde{m}}_i \tilde{V}_i^2 + \frac{3}{2} \frac{k_{\rm B}}{\mu} \tilde{\tilde{m}}_i \tilde{T}_i - \frac{GM}{r_i} \tilde{\tilde{m}}_i . \tag{B8}$$

The filtered-solution then serves as the starting point for the next time step. This process conserves the total mass but yields a mild nonconservation of energy and momentum.

REFERENCES

Aizu, K. 1973, *Progr. Theor. Phys.*, **49**, 1184.
Allen, C. W. 1973, *Astrophysical Quantities*, (3d ed.; London: Athlone).
Bond, H. E., Chanmugam, G., and Grauer, A. D. 1979, *Ap. J. (Letters)*, **234**, L113.
Cameron, A. G. W., and Mock, M. 1967, *Nature*, **215**, 464.
Chanmugam, G., and Wagner, R. L. 1979, *Ap. J.*, **232**, 895.
Chiappetti, L., Tanzi, E. G., and Treves, A. 1980, *Space Sci. Rev.*, **27**, 3.
Davidson, K. 1973, *Nature Phys. Sci.*, **246**, 1.
Fabbiano, G., Hartmann, L., Raymond, J., Steiner, J., Branduardi-Raymont, G., and Matilsky, T. 1981, *Ap. J.*, **243**, 911.
Fabian, A. C., Pringle, J. E., and Rees, M. J. 1976, *M.N.R.A.S.*, **175**, 43.
Field, G. B. 1965, *Ap. J.*, **142**, 531.
Giacconi, R., Gursky, H., Kellogg, E., Schreier, E., and Tananbaum, H. 1971, *Ap. J. (Letters)*, **167**, L67.
Hamada, T., and Salpeter, E. E. 1961, *Ap. J.*, **134**, 683.
Harten, A., and Zwas, G. 1972, *J. Eng. Math.*, **6**, 207.
Hearn, D. R., and Richardson, J. A. 1977, *Ap. J. (Letters)*, **213**, L115.
Hōshi, R. 1973, *Prog. Theor. Phys.*, **49**, 776.
Katz, J. J. 1977, *Ap. J.*, **215**, 265.
King, A. R., and Lasota, J. P. 1979, *M.N.R.A.S.*, **188**, 163.

Kiplinger, A. L. 1979, *Ap. J.*, **234**, 997.
Kylafis, N. D., and Lamb, D. Q. 1979, *Ap. J. (Letters)*, **228**, L105.
Lamb, D. Q., and Masters, A. R. 1979, *Ap. J. (Letters)*, **234**, L117.
Lamb, F. K., Pethick, C. J., and Pines, D. 1973, *Ap. J.*, **184**, 271.
Langer, S. H., Chanmugam, G., and Shaviv, G. 1981, *Ap. J. (Letters)*, **245**, L23 (Paper I).
Langer, S. H., and Rappaport, S. 1982, *Ap. J.*, **257**, in press.
Masters, A. R. 1978, Ph.D. thesis, University of Illinois, Urbana.
Middleditch, J. *Bull. AAS*, **13**, 816.
Panek, R. J. 1980, *Ap. J.*, **241**, 1077.
Patterson, J., Branch, D., Chincarini, G., and Robinson, E. L. 1980, *Ap. J. (Letters)*, **240**, L133.
Patterson, J., and Price, C. M. 1981, *Ap. J. (Letters)*, **243**, L83.
Pringle, J. E., and Savonije, G. J. 1979, *M.N.R.A.S.*, **187**, 777.
Rappaport, S., Cash, W., Doxsey, R., McClintock, J., and Moore, G. 1974, *Ap. J. (Letters)*, **187**, L5.
Raymond, J. C., Black, J. H., Davis, R. J., Dupree, A. K., Gursky, H., Hartman, L., and Matilsky, T. A. 1979, *Ap. J. (Letters)*, **230**, L95.
Ricketts, M. J., King, A. R., and Raine, D. J. 1979, *M.N.R.A.S.*, **186**, 233.

Rothschild, R. E., *et al.* 1981, *Ap. J.*, **250**, 723.
Rotty, R. M. 1962, *Introduction to Gas Dynamics* (New York: Wiley).
Schmidt, G. D., Stockman, H. S., and Margon, B. 1981, *Ap. J. (Letters)*, **243**, L157.
Spitzer, L. 1956, *Physics of Fully Ionized Gases* (New York: Interscience).
Tuohy, I. R., Lamb, F. K., Garmire, G. P., and Mason, K. O. 1978, *Ap. J. (Letters)*, **226**, L17.
Visvanathan, N., and Wickramasinghe, D. T. 1979, *Nature*, **281**, 47.
Wada, T., Shimuzu, A., Suzuki, M., Kato, M., and Hōshi, R. 1980, *Prog. Theor. Phys.*, **64**, 1986.

G. CHANMUGAM: Department of Physics and Astronomy, Louisiana State University, Baton Rouge, LA   70803

S. H. LANGER: Department of Astronomy, University of Illinois, Urbana, IL   61801

G. SHAVIV: Faculty of Physics, Israel Institute of Technology, Haifa, Israel   32000